iScience

Article

A graphene-based photo-electro-thermal metamaterial for soft fixtures with superior grasping performance

Graphical abstract

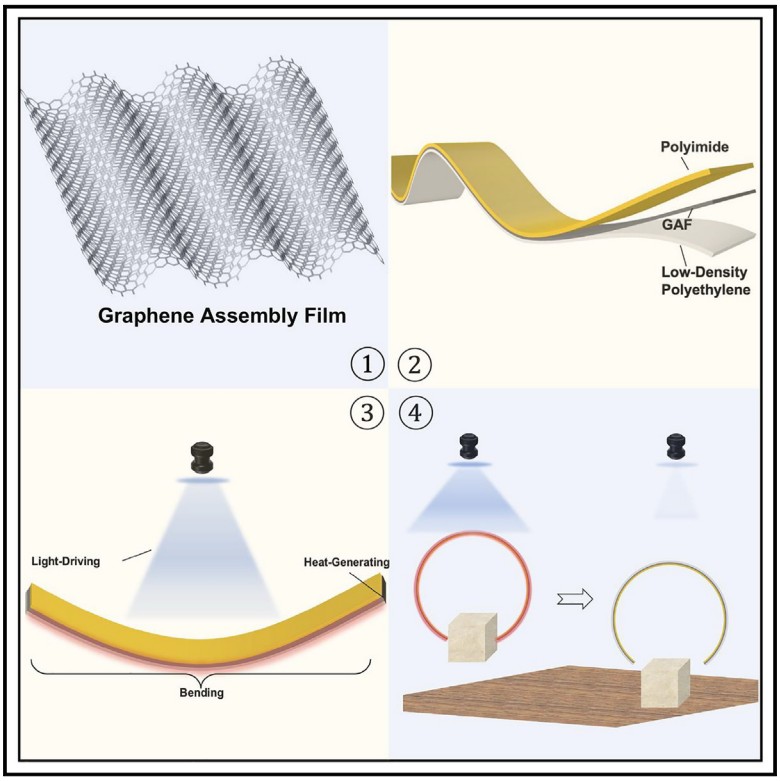

Authors

Bowen Yang, Xuanchen Dong, Wenhao Lv, ..., Tonghui Lu, Xianglin Li, Song Lv

Correspondence

lvsong@whut.edu.cn

In brief

Natural sciences; Physics; Applied sciences

Highlights

- Graphene-assembled film (GAF) enhances photothermal efficiency and strength
- Sandwich-structured-metamaterial (SSM) with GAF shows superior curvature and strength
- SSM fixtures are energy efficient and lift objects approximately eight times their own weight

Yang et al., 2025, iScience *28*, 111743
February 21, 2025
https://doi.org/10.1016/j.isci.2025.111743

CellPress

iScience

CellPress
OPEN ACCESS

Article

A graphene-based photo-electro-thermal metamaterial for soft fixtures with superior grasping performance

Bowen Yang,[1] Xuanchen Dong,[1] Wenhao Lv,[2] Wenzhuo Liu,[1] Mengying Lu,[1] Zhe Liu,[1] Tonghui Lu,[1] Xianglin Li,[1] and Song Lv[1,2,3,*]

[1]School of Naval Architecture, Ocean and Energy Power Engineering, Wuhan University of Technology, Wuhan 430063 China
[2]School of Materials Science and Engineering, Wuhan University of Technology, Wuhan 430063 China
[3]Lead contact
*Correspondence: lvsong@whut.edu.cn
https://doi.org/10.1016/j.isci.2025.111743

SUMMARY

Soft actuators are valued for their adaptability and diverse applications but often face challenges like slow response, high activation energy, and high energy consumption. To address these issues, we developed a graphene-assembled film (GAF) via the redox method, characterized by high thermal conductivity, conductivity, and stiffness. Using GAF as a photothermal and electrothermal driver, we engineered a sandwich-structured metamaterial (SSM) by combining two polymers with vastly different thermal expansion coefficients. The SSM achieved rapid response (<5 s), low actuation energy ($\leq$0.22 W cm^{-2} or $\leq$3.55 V), and large bending curvature (>0.18 mm^{-1}), surpassing conventional designs in response speed (226.2% faster) and curvature (249.1% higher). This metamaterial enables soft fixtures with superior gripping capabilities and low energy consumption, handling up to eight times the object mass of traditional designs. This work highlights advances in multi-stimulus metamaterials, offering significant implications for the development of high-performance soft actuators.

INTRODUCTION

In the contemporary world, there is an urgent need for soft actuators that demonstrate superior adaptability, flexibility, and safety.[1] This demand is rapidly emerging across various applications, from wearable devices[2] to extreme environments like the deep sea, where traditional rigid devices are unsuitable.[3] Soft actuators are typically made from soft materials such as silicone,[4] polymers,[5] or hydrogels[6] and do not require batteries, information processing units, electronic circuits, motors, or transmission mechanisms.[7] This greatly simplifies their structure and improves their practicality and adaptability to extreme environments.[8]

Recently, various soft actuators have achieved multiple functionalities, such as swimming,[9] crawling,[10] and walking,[11] through single-mode actuation. However, studies on actuators demonstrating excellent grasping performance are still relatively scarce. Some research has employed grippers made of azobenzene materials that undergo photoisomerization,[12] achieving rapid response through photochemical reactions, but with a limited gripping mass of 12 mg. Other studies have used grippers made from highly conductive slidable silver nanowires[13] with strong mechanical properties, achieving breakthroughs in gripping mass (182 mg) at the cost of higher energy consumption. Both approaches rely solely on a single light energy drive, lacking stability and facing challenges in further improving energy efficiency. Therefore, developing a multi-stimulus-driven metamaterial that can handle larger mass objects while consuming minimal energy remains a pressing issue to be addressed.

Metamaterials, especially their programmability, have emerged as a promising direction in the field of flexible actuators. The programmable characteristics of metamaterials can be realized through both active and passive methods.[14] In active programming, materials respond to external stimuli (such as light, electricity, magnetic fields, etc.) to alter their properties or morphology.[15] For example, photoisomerization materials[16] and highly conductive nanowire materials[17] have been used to develop actuators driven by light or electrical signals, but they still face challenges related to energy consumption and stability. In contrast, passive programming relies on the inherent multi-physical properties of materials.[18] Through the design and modulation of the microstructure or composition of the material, it can exhibit predetermined performance under specific conditions. For instance, some studies utilize the anisotropic design of materials to achieve specific mechanical properties,[19] whereas others exploit differences in thermal expansion coefficients or thermal conductivity to realize functional changes.[20] Such passive programming methods typically enable efficient functional transformation without external energy input, offering higher energy efficiency and lower operational complexity.

Graphene, due to its high thermal conductivity,[21] high electrical conductivity,[22] and high rigidity,[23] has shown great potential

in the programmable characteristics of metamaterials. However, pristine graphene exhibits high transparency, low photothermal efficiency, poor thermal stability, and a low coefficient of thermal expansion[24] (CTE), which is insufficient to facilitate photothermal actuation. To address these limitations, we designed and fabricated a graphene assembly film (GAF) using a redox method, inducing large-scale alignment through compression. The microstructure of GAF exhibits a multilayered stacking pattern that resolves the issue of high transparency found in pristine graphene. This structure increases the surface area, allowing for more effective light trapping within the material and extending the residence time of photons, thereby enhancing photothermal conversion efficiency.[25] Additionally, the structure effectively disperses externally applied stresses, inhibits crack propagation, and increases surface roughness, significantly enhancing its mechanical strength.[23] Experimental measurements have shown significant improvements in the thermal stability and photothermal efficiency of GAF.

Given the low CTE and excellent photothermal conversion efficiency of GAF, we embedded it as a heat-driven material into two polymer materials with a significant difference in CTEs (an average difference of up to 850 times; Table S1). The GAF layer is sandwiched between two polymer materials, polyimide (PI) and low-density polyethylene (LDPE). When energy is input into the actuator, the GAF layer generates significant heat. Due to the large difference in CTEs between the polymer layers, the entire actuator bends toward the side with a lower thermal expansion coefficient, resolving the issue of actuation with graphene materials. We refer to this graphene-based sandwich-structured material as "sandwich-structured metamaterial" (SSM). The results demonstrate that this SSM material not only allows for active programming through multiple external stimuli such as light, heat, and electricity but also enables passive response via the material's thermal expansion properties. The large-scale alignment induced by compression achieves significant photothermal conversion efficiency and superior mechanical performance, including rapid response (time from the onset of bending to maximum curvature being less than 5 s, driven by light intensity $\leq 0.22\ W\ cm^{-2}$ or voltage ≤ 3.55 V), large curvature ($>0.18\ mm^{-1}$), and high stiffness (Young's modulus >10 MPa). Compared to conventional strategies,[26] the response time is reduced by 226.2%, and the curvature increases by 249%. The developed fixtures consume less energy (with activation light intensity on average 325% lower than in conventional studies[27,28]), exhibit exceptional grasping capabilities (the mass of objects is up to eight times that of traditional researches[29,30]), and demonstrate significantly enhanced energy efficiency (the mass-to-energy consumption ratio is 10 times higher than the currently reported optimal values[31,32]), closely aligning with our predefined criteria and expectations.

At the end, we demonstrated other applications of SSM, such as serving as a thermometer with a measurement range from 20°C to 70°C or enabling mobility behaviors, where within 10 s, the bending angle changes by approximately 200°. These superior performances determine the wide application potential of SSM. In extreme environments, such as high-pressure deep-sea conditions, the soft structure of SSM facilitates the capture of tiny objects. It can also be applied in wearable devices by embedding SSM in certain parts of clothing to create breathable mechanisms. Environmental light or a rise in body temperature during exercise can promote the operation of SSM, forming multiple small holes in the underlying cotton fabric to allow for breathability. This study has achieved innovative results in metamaterials driven by multi-stimulus response behavior and has made significant progress in the performance of soft fixtures, advancing the development of soft actuators.

RESULTS

Preparation and testing of GAF

Graphene is a two-dimensional material composed of a single layer of carbon atoms arranged in a hexagonal lattice.[33] It is renowned for its exceptional electrical, thermal, and mechanical properties.[22] Graphene exhibits high electrical conductivity,[34] excellent thermal conductivity, and remarkable mechanical strength,[21] making it a promising material for a wide range of applications, including electronics, energy storage, and composite materials.

However, pristine graphene, in its original form, has several limitations that can affect its photothermal effect. The surface state of graphene has a significant impact on its photothermal conversion efficiency. The surface of pristine graphene has not been optimized, resulting in lower light absorption and thermal conductivity compared to functionalized or modified graphene.[35] Additionally, defects and impurities introduced during synthesis can significantly impact the material's electronic structure and optical properties.[36] These defects can lead to uneven absorption and scattering of light, further reducing the photothermal conversion efficiency. Thus, although graphene holds great potential for photothermal applications, these limitations need to be addressed through improved synthesis methods and post-processing techniques to optimize its performance.

Herein, we report a method for the preparation of graphene films. For the detailed preparation process, see the STAR Methods section. (Figure 1A). Following this procedure, a complete GAF can be prepared. The shape, morphology, micro-surface, and cross-section of the GAF are depicted in Figures 1B and 1C. Subsequently, the composition and quality of the fabricated graphene film are subjected to testing and analysis. The Raman spectrum of the prepared graphene, depicted in Figure 1D, serves as a pivotal analytical tool for discerning the carbon defect density inherent within the material. Specifically, the distinct vibrational bands of D, G, and G′ manifest at 1,336.6 cm^{-1}, 1,585.6 cm^{-1}, and 2,679.3 cm^{-1}, respectively. The D band denotes the presence of defective carbon species within the residual carbon lattice, whereas the G band signifies the abundance of graphitic carbon structures within the residue. Notably, the attenuated intensity of the D peak juxtaposed with the augmented intensities of the G and G′ peaks intimate a graphene structure with diminished defect density and a pronounced SP2-hybridized carbon framework.

Furthermore, the assessment in Figure 1E, entailing the fitting of Raman spectra of graphene oxide pre- and post-reaction, yields the ID/IG intensity ratio. This ratio, a surrogate for the carbon residue's defect density, manifests a direct association with the graphite crystallite dimensions (La), as delineated by the

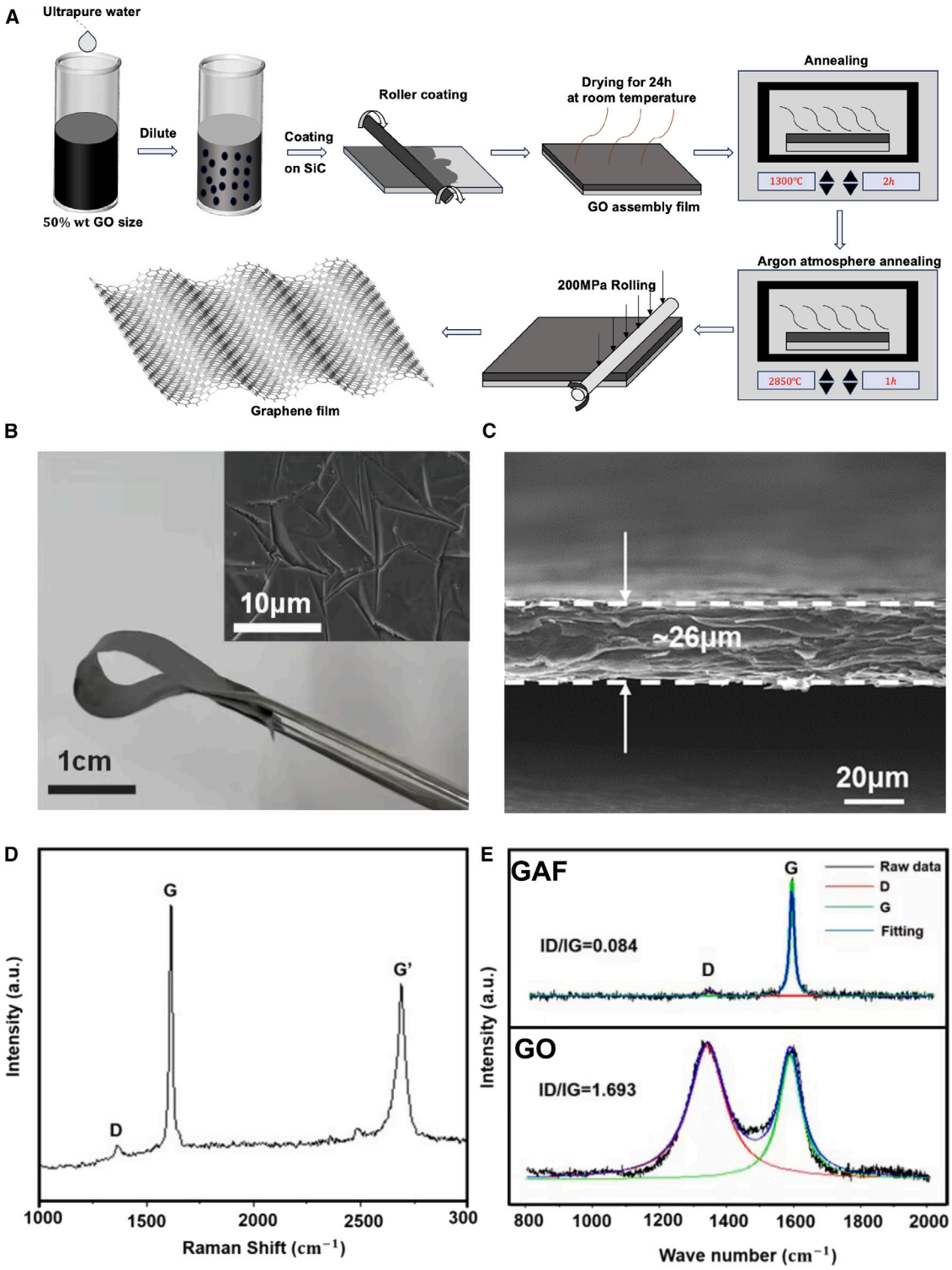

Figure 1. The production process, microscopic morphology, and quality testing of GAF

(A) Schematic illustration of the procedure for graphene assembly films.

(B) A digital photo of graphene film. A scanning electron microscope image inset shows many micro folds on the surface of graphene film. The scale bar is 1 cm.

(C) The cross-sectional SEM image of graphene film. The scale bar is 20 μm.

(D) The Raman spectrum of the prepared graphene.

(E) The comparison of the Raman spectra between prepared graphene and graphene oxide indicates that prepared graphene has a higher degree of graphitization.

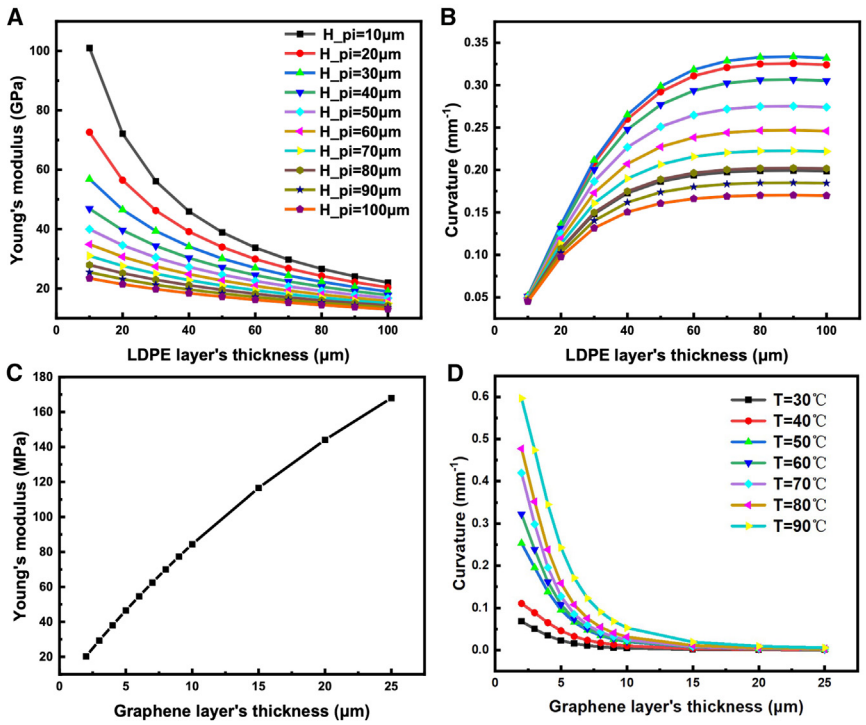

Figure 2. The selection process for the thickness of each layer in the SSM

(A) Variation of the PI/Graphene/LDPE sandwich-structured actuator's Young's Modulus with polymer's thickness, when the temperature is 70°C, the thicknesses of graphene is 5 μm.

(B) Variation of the PI/Graphene/LDPE sandwich-structured actuator's curvature with polymer's thickness, when the temperature is 70°C, the thicknesses of graphene is 5 μm.

(C) Variation of the PI/Graphene/LDPE sandwich structured actuator's Young's Modulus with graphene thickness, when the temperature is 70°C, the thicknesses of LDPE and PI are 20 μm and 30 μm, respectively.

(D) Variation of the PI/Graphene/LDPE sandwich-structured actuator's curvature with graphene thickness, when the temperature is from 30°C to 90°C, the thicknesses of LDPE and PI are 20 μm and 30 μm, respectively.

Tuinstra-Koenig correlation: ID/IG = 4.35/La. Consequently, a reduced ID/IG ratio connotes an enhanced degree of carbon atom alignment. Notably, the observed transition in the ID/IG ratio from 1.69 to 0.084 signifies the transformation from disordered carbon atom configurations inherent in graphene oxide to a substantially ordered arrangement characteristic of graphene. Comprehensive X-ray photoelectron spectroscopy (XPS) analysis in Figure S1 is conducted on both the graphene film and graphene oxide film. The occurrence of the redox reaction is confirmed, affirming the success of the redox method in the synthesis of graphene.

Henceforth, it is evident that the graphene film fabricated in this study exhibits a high degree of graphitization, characterized by reduced defects and a more ordered arrangement of carbon atoms. Such structural attributes endow graphene with enhanced capability to efficiently absorb and convert light energy,[24] thereby demonstrating superior photothermal performance. Consequently, it emerges as an exemplary photothermal driving material within sandwich composite materials.

Determination of layer thicknesses in SSM

The bilayer structure, comprising a photoactive and a photo-passive layer, holds great promise for designing photo-responsive soft actuators.[37] By selecting materials with diverse chemical structures and mechanical properties, a variety of photo-responsive soft actuators can be constructed, offering ultra-sensitivity, programmability, and excellent compatibility.[38] Although traditional approaches involve incorporating molecular photoswitches (e.g., azobenzene)[39] or photothermal nanomaterials (e.g., Au)[40] into a soft matrix, simplification has been sought by directly using compounds with these properties as the photoactive layer.[41] However, achieving stable actuation performance, especially in challenging conditions like low temperatures and extreme deformations, remains a hurdle due to weak interfacial interactions between the layers. Streamlining the fabrication process is crucial for real-world applications.

To address the constraints, a straightforwardly fabricated and highly stable SSM has been proposed. It is composed of PI, GAF, and LDPE where PI and LDPE layers are procured directly. The selection of these two materials is considering the excellent thermal stability, dimensional stability, and high mechanical strength of PI and the flexibility and ease of processing characteristics of LDPE. Most importantly, their average coefficients of thermal expansion (CTEs) differ by a factor of 850 between 20°C and 90°C,[42] enabling the sandwich-structured material to undergo directional bending upon absorbing energy and temperature elevation.

Before fabricating the sandwich-structured actuator, it is imperative to conduct certain simulation calculations to approximately estimate the optimal thickness of each layer, as the thickness of each layer directly influences the final actuator's performance such as the Young's modulus and curvature of the entire system. In Figures 2A and 2B, numerical calculations are initially employed to determine the relatively optimal thicknesses of the PI and LDPE layers. From Figures 2A and 2B, it can be seen that as the thickness of the LDPE layer increases, the system's Young's modulus decreases and the curvature increases. When the thickness of the PI layer increases, the system's Young's modulus decreases as well. Notably, when the PI layer thickness is 30 μm, the system's curvature reaches its peak value. The final thickness of the PI layer is determined to be 30 μm and the LDPE layer's to be 20 μm.

The determination of the most crucial layer thickness, graphene, is depicted in Figures 2C and 2D. Although maintaining the thickness of the remaining two layers unchanged, variations

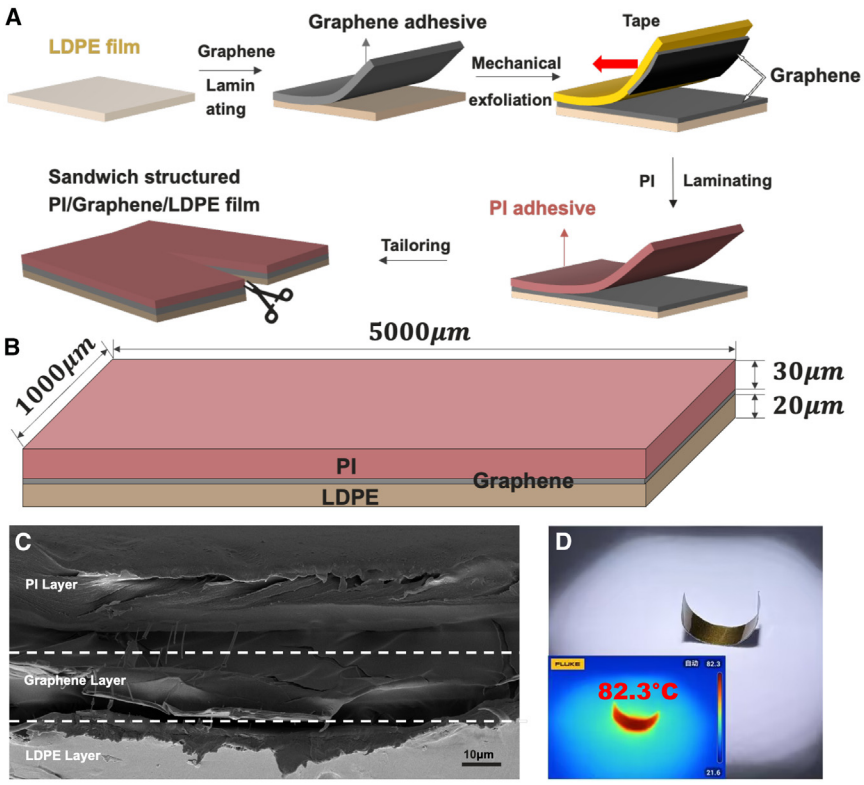

Figure 3. The preparation process, macroscopic and microscopic shape characterization, and thermal stability testing of SSM

(A) Schematic illustration of the procedure for fabricating PI/Graphene/LDPE composite films.

(B) Components and dimensions of the PI/Graphene/LDPE SSM.

(C) The cross-sectional SEM image of the SSM. The scale bar is 10 μm.

(D) The stability testing of the metamaterial under intense illumination. Inset shows IR thermal image of the highest temperature of the whole process.

in the graphene layer thickness are investigated to obtain the curvature and Young's modulus of the SSM as functions of the graphene layer thickness. It is observed that as the graphene layer thickness increased, the curvature of the SSM decreased while the Young's modulus increased. In order to meet all the requirements, a thickness of 6 μm is chosen for the graphene layer.

Fabrication of SSM

Using LDPE as the substrate, a graphene film is prepared and attached to the substrate. The lamination method is employed to combine different materials. Due to the excessive thickness of the graphene film, which fails to meet the requirements for actuation, the mechanical exfoliation is employed on the surface of the graphene film to reduce its thickness. This method can ensure that the thickness of each layer produced is not more than 500 nm different from the simulation result. Then, a PI layer is fixed onto the surface of the graphene, resulting in a SSM with excellent photothermal properties and actuation capabilities (Figure 3A). The fabrication process offers reproducibility, enabling variation in layer thickness to achieve diverse properties, showcasing remarkable controllability. The dimensions, appearance, morphology, and microstructure of the SSM are depicted in Figures 3B and 3C, with particular emphasis on its exceptional photothermal performance and thermal stability, notably evident in Figure 3D.

Performance testing of SSM

According to the previously mentioned principles, when the graphene layer serving as the thermally driven layer is subjected to light irradiation or electrical stimulation, it generates heat. Due to the significant difference in thermal expansion coefficients between the materials on the upper and lower layers of the graphene, the sandwich-structured actuator bends toward the side (PI layer) with the smaller thermal expansion coefficient (Figure 4A). Consequently, the actuators fabricated according to the aforementioned layer thicknesses are exposed to xenon lamp irradiation (Figure 4B). The results indicate a rapid response, with considerable bending occurring in less than 10 s (Video S1). Curvature changes throughout the process are recorded, with ImageJ analysis confirming alignment with theoretical calculations (Figure S3).

At the same time, the actuator is exposed to a direct current of 3.55 V and 0.22 A applied to the graphene layer pasted with copper foil. In this scenario, the actuator exhibits substantial bending in less than 5 s, demonstrating excellent performance metrics, including a large deformation range (curvature >0.11 mm^{-1}), rapid response (<5 s), and low actuation voltage ($\leq$3.6 V) (Figure 4C and Video S2).

The temperature variations during the process are measured in Figure 4D. One significant challenge hindering the widespread adoption of soft actuators is their relatively limited mechanical performance.[43] Tensile tests are conducted on SSMs of varying thicknesses to obtain their stress-strain curves. As depicted in Figure 4E, when the GAF layer thickness is 6 μm, the elastic modulus of the SSM is approximately 10 MPa, whereas with a GAF layer thickness of 10 μm, the elastic modulus of the SSM increases to approximately 14 MPa. The presence of GAF imparts remarkable physical properties to the material, including enhanced mechanical strength, toughness, excellent fatigue resistance, and long-term repeatability. Furthermore, five repeated experiments are conducted on the SSM shown in Figure 4F, confirming that the surface experimental results are not incidental and indicating the material's potential for repeatable use.

Soft fixtures based on SSM

Following the aforementioned fabrication process, a series of PI/Graphene/LDPE sandwich-structured actuators are produced.

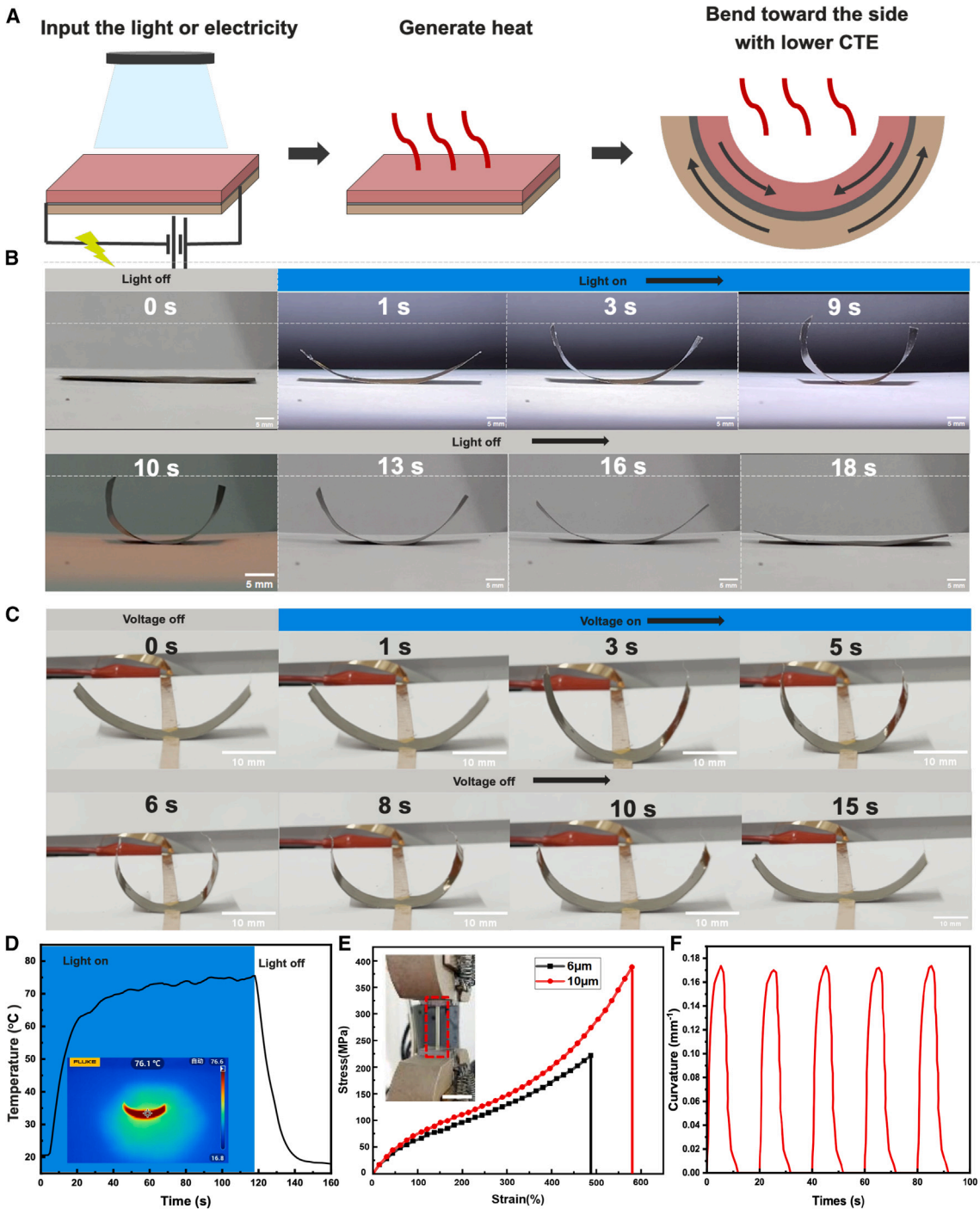

Figure 4. Physical properties of sandwich structured metamaterials under optical and electrical driving

(A) Schematic illustration of the sandwich structured actuator bent by photothermal or electric heating.

(B) Real-time optical images showing light-induced actuation xenon lamp irradiation (242 mW cm^{-2} as mean ± 8.5%). The scale bar is 5 mm.

(C) Optical images demonstrating electrically induced actuation, with the actuator rolling upon application of 3.55 V (as mean ± 5.1%) voltage and returning to its original state after voltage cessation. The scale bar is 10 mm.

(D) Temperature change during illumination induced actuation, with corresponding IR thermal image.

(E) Stress-strain curves of SSM with graphene thicknesses of 6 μm and 10 μm (measurement errors are ±5.4%).

(F) Repeatability testing of SSM.

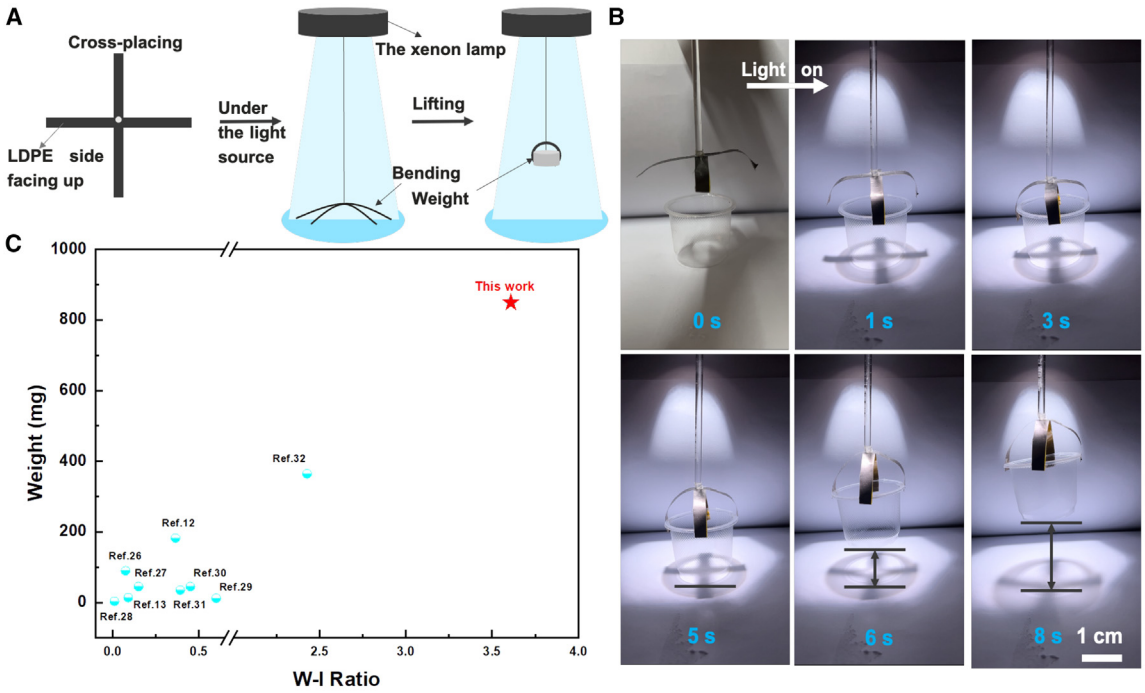

Figure 5. Practical applications of fixtures fabricated from sandwich-structured metamaterials comparison of grasping performance with other studies

(A) Schematic illustration of the fixture consisted of the PI/Graphene/LDPE sandwich-structured actuators grabbing process.

(B) Optical images of the whole process of grasping objects upon exposure to the light source with intensity of 235.4 mW cm^{-2} (±8.5%). The scale bar is 1cm.

(C) The weight-intensity ratio characteristic comparison between this work and previous studies.

Two identical actuators are affixed together in a cross formation, aligning the LDPE side upward. This combined structure is suspended under a light source using a string. Upon activating the light source, the combination undergoes downward bending influenced by gravity and the photothermal effect (Figure 5A). A half plastic cup is strategically positioned beneath the actuator assembly, and the rope is gradually lowered. As the actuator exhibits significant bending, it engages with the weight, enabling the lifting of the load. This sequential process demonstrates the actuator's grasping capabilities effectively (Figure 5B and Video S3).

The straightforward combination of the PI/Graphene/LDPE composite actuator into a fixture holds significant performance (Figure S4). Here, two parameters regarding gripping performance are compared: one is the weight of the gripped object, and the other is a custom parameter called the W-I Ratio, which is the ratio of the gripping mass to the energy input (light intensities and near-infrared [NIR] for all studies) during the gripping process. The larger this parameter, the higher the energy utilization efficiency. In comparison to previous studies[12,13,26–32] (Table S2), the W-I Ratio of this work is 1.2 times that of the best and 18 times that of the conventional. The mass of the lifted object in this work is twice that of the best and eight times that of the conventional (Figure 5C). In other words, the soft fixture in this work lifted the heaviest object and achieved the highest energy conversion efficiency among similar studies.

A visual thermometer based on SSM

Based on the fundamental principles of the photothermal effect micro-actuator, a marine miniature actuator has been designed for temperature measurement within a ship's cabin. Finite element software was employed to simulate the bending behavior of the temperature-indicating thin film within the temperature range of 10°C–90°C, as depicted in Figure 6A. A detailed description of the simulation process is provided in Figure S5. It is evident from the figure that at 20°C, the designated initial temperature for the temperature-indicating film, the film remains flat. When the temperature drops below 20°C, the film bends downward, whereas temperatures above 20°C cause the film to bend upward. At 90°C, the film bends significantly, forming a shape nearly resembling a complete circle. Subsequently, at higher temperatures, the film undergoes further bending and contraction, gradually reducing the circular shape as the temperature increases.

As illustrated in Figure 6B, the structure of the marine miniature actuator consists of two main components: a temperature scale plate and a long strip-shaped temperature-indicating thin film. Given the potential for insufficient illumination inside the cabin, a layer of red fluorescent paint is applied to the surface of the thin film to facilitate clear observation of its bending state. By inputting optical energy into the SSM, different temperature environments are generated. The experimental results indicate that the operational performance of the thermometer aligns closely with the expectations, demonstrating practical utility.

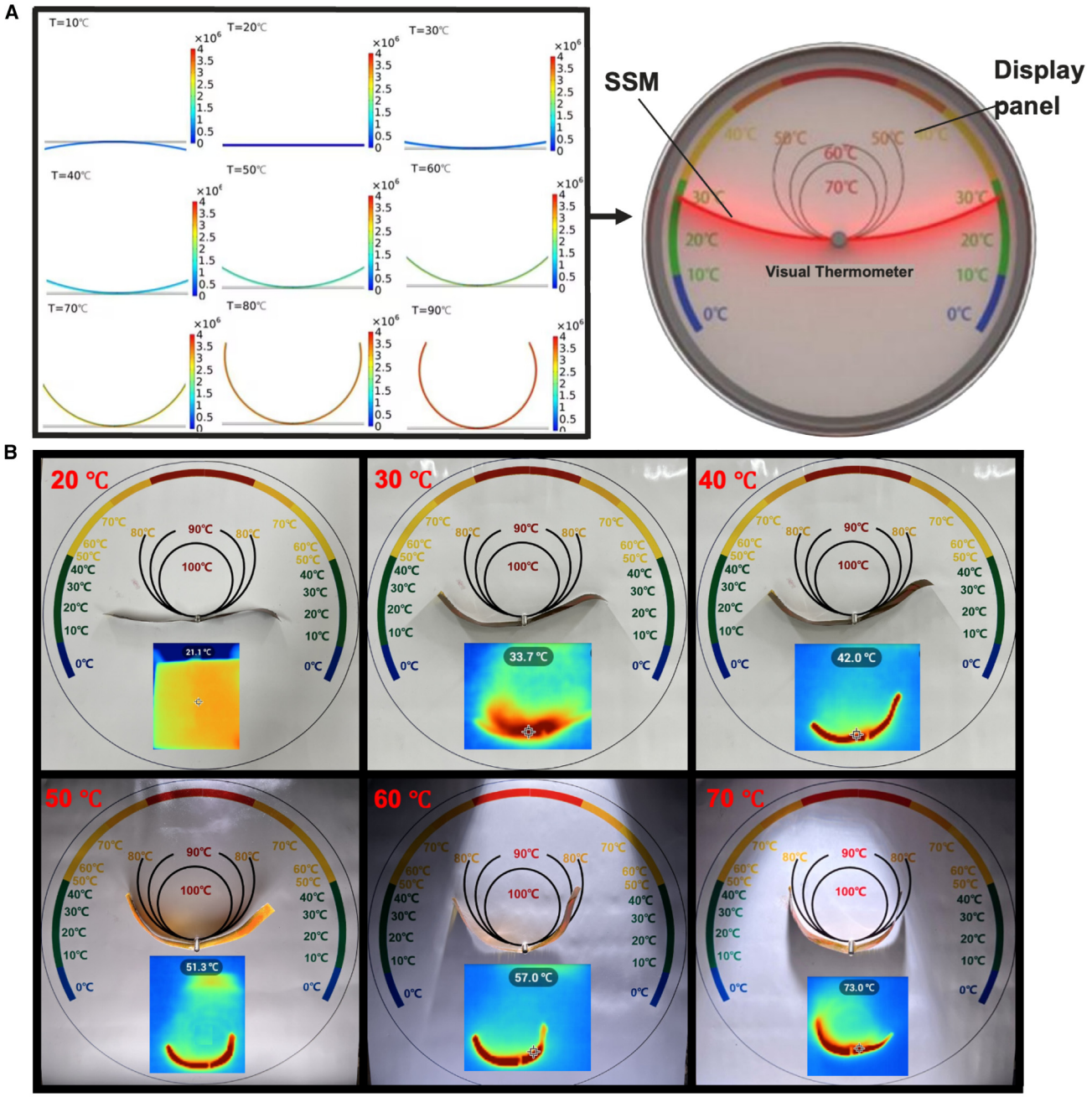

Figure 6. Practical implementation of a thermometer based on sandwich-structured metamaterials

(A) The approximate bending behaviors of the thermometer at different temperatures obtained through finite element software simulation and schematic illustration of the thermometer based on SSM.

(B) The indication of the thermometer at different temperatures ranging from 20°C to 90°C with corresponding infrared thermal images (measurement errors of temperatures are ±7.9%).

However, two points regarding the practical application of the thermometer require further clarification. First, the reported thermometer has limited accuracy and can only estimate approximate temperatures. Second, due to the constraints posed by the thickness of the metamaterial graphene layer used in the thermometer, repeated experiments have shown that its maximum achievable temperature is approximately 70°C. The simulation results illustrate an extreme scenario that cannot be fully realized in practice.

Rotational motion based on SSM

Notably, a counterintuitive phenomenon is observed with the further reduction of graphene layer thickness (Figure S6). In the

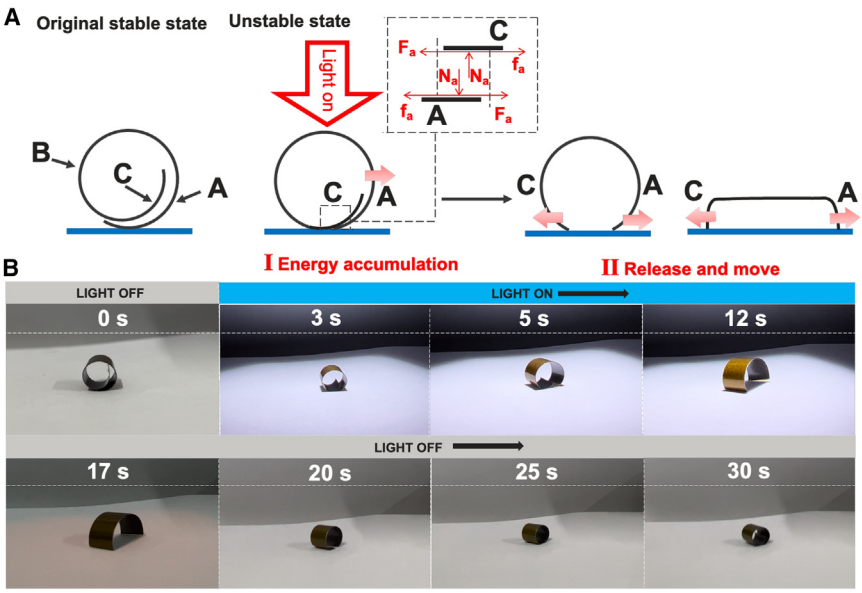

Figure 7. An actuator undergoing a process from rolled to flat, which is completely opposite to its previous actuation behavior

(A) Schematic illustration of the moving model that contains the stable state and the unstable state. Without light irradiation, it keeps stable. In the unstable state, the light-driven jumping process includes (I) energy accumulation and (II) release and move.

(B) Optical images of the entire jumping motion process of the robot under the light irradiation.

absence of external energy input, the actuator naturally assumes a curved state. However, exposure to light at an intensity of 235.4 mW cm^{-2} prompts the actuator to flatten, demonstrating significant movement throughout the process.

In Figure 7A, the actuator is divided into three parts (labeled as "A", "B", and "C") forming a closed loop, with the ends ("A" and "C") overlapping, and a schematic diagram of the movement model is provided. This model includes the stable state before illumination and the unstable state after illumination. When the mobile robot is placed on the ground without light stimulation, it maintains the tubular shape with "A" and "C" overlapping. In this initial stable state, there is almost no force between "A" and "C". Under illumination from top to bottom, the area of the robot facing the light (including parts of "B" and "A") begins to unfold and tends to straighten, causing a change in the curvature of the loop. However, the photothermal expansion of "A" and "B" is temporarily blocked by the undeformed region "C" that is not illuminated. In this energy-accumulated unstable state, "A" and "C" are in close contact (Figure 7AI). The light-induced bilayer expansion results in the normal force N_a, shear force F_a, and overall friction force f_a at the A-C contact surface, as shown in the dashed rectangular inset in Figure 7A. When $F_a = f_a$, there is no relative movement at the A-C contact surface.

As the illumination time increases, thermal expansion also increases accordingly, leading to an increase in the stored strain energy in the bilayer actuator and an increase in the shear force F_a. When F_a increases to a certain point where it exceeds the maximum static friction force, i.e., $F_a > f_a$, relative motion begins at the A-C contact surface, and the contact friction force f_a transitions from static friction to the smaller kinetic friction. The relative motion between the surfaces of "A" and "C" reduces the contact area. When the accumulated energy increases to a level that causes the separation of "A" and "C", the strain energy stored in the actuator is suddenly released at the moment A-C loses contact, converting into kinetic energy and impact energy against the ground (Figure 7AII). Under the combined effect of the instantaneous ground reaction force and converted kinetic energy, a motion of the robot is generated. Optical images of the entire light-induced motion at different times are also shown in Figure 7B. After the light stimulation is turned on, the robot remains essentially stationary for the first 3 s while strain energy accumulates. After continuous illumination for about 3.6 s, the motion suddenly starts due to the instantaneous release of the accumulated strain energy. Video S4 provides the video of the entire movement process.

Based on the aforementioned characteristics of the actuator, a potential application scenario for an adaptive soft robot in underwater exploration can be envisioned. This robot could be employed for temperature sensing and micro-scale detection tasks in marine environments. Due to its photothermal actuation mechanism, the robot does not require complex electrical power supplies or external control systems; it can be activated solely through environmental light or directed light sources. In practical applications, the robot could adjust its shape and position in response to changes in ocean temperatures, enabling precise monitoring or data collection in specific areas.

This robot is particularly suited for operation in narrow underwater crevices or inaccessible deep-sea environments, where its flexibility and adaptability allow it to traverse complex terrain structures and adjust autonomously based on environmental changes. Its self-actuating capability makes it ideal for long-term exploration tasks, utilizing natural underwater light sources or installed illumination systems. Such robots hold significant potential for marine research, environmental monitoring, and underwater archaeology, offering a versatile and energy-efficient solution for various challenging underwater missions. The practical implementation of these applications warrants further exploration and experimentation.

DISCUSSION

In this study, we successfully fabricated GAFs using a redox method, achieving large-scale alignment through compression and developing a multilayered stacking microstructure. This design enhances photothermal conversion efficiency by increasing surface area and photon residence time, while also improving mechanical properties and stress dispersion. These improvements address the key limitations of pristine

graphene, such as high transparency and low mechanical strength.

We embedded GAFs as heat-driven materials into SSMs composed of PI and LDPE, chosen for their substantial difference in CTEs. This configuration achieved significant actuation capabilities, including rapid response times and high curvature, with minimal energy input. Compared to conventional strategies, our SSM exhibited a 226.2% reduction in response time and a 249% increase in curvature, highlighting its superior efficiency and performance.

The application scope of SSMs extends beyond basic actuation. We particularly demonstrated the exceptional performance of SSMs as soft fixtures. By connecting two identical SSM actuators in a crossed configuration with the LDPE side facing upward and suspending them under a light source, the assembly bent downward under the influence of gravity and photothermal effects, thereby demonstrating its gripping ability. Experimental results showed that this soft fixture could handle objects weighing up to eight times more than those managed by traditional designs, with a 10-fold increase in energy conversion efficiency.

Overall, this study represents a significant advancement in the development of photothermal-driven metamaterials, pushing the boundaries of soft actuator technology. Future research should focus on optimizing the interface interactions within SSMs to further enhance stability and performance under various environmental conditions. Additionally, exploring other material combinations and structural configurations could lead to even more efficient and versatile soft actuators, broadening their application scope in both industrial and consumer products.

Limitations of the study

Despite exploring various approaches, the study faced a significant limitation in achieving underwater grasping. The temperature difference, which was initially used as a driving factor, quickly dissipated at the moment the actuator entered the water, leading to a rapid loss of effectiveness. As a result, underwater grasping could not be successfully achieved in this study. Further efforts and improvements are required to overcome this challenge and accomplish the desired results in future work.

RESOURCE AVAILABILITY

Lead contact

Requests for further information and resources should be directed to the lead contact, Song Lv (lvsong@whut.edu.cn).

Material availability

This study did not generate new unique reagents.

Data and code availability

- All data can be obtained from the lead contact, provided the request is reasonable.
- The code related to the developed model can be accessed by reaching out to the lead contact.
- Any additional information required to reanalyze the data reported in this paper is available from the lead contact upon request.

ACKNOWLEDGMENTS

This study was sponsored by the National Natural Science Foundation of China (NSFC52106268) and the National Natural Science Foundation of Hubei Province, China (No. 2022CFB316).

AUTHOR CONTRIBUTIONS

B.Y., X.D., and W.L., substantial contributions to the conception or design of the work or the acquisition, analysis, or interpretation of data for the work; W.L., M.L., Z.L., T.L., and X.L., drafting the work or revising it critically for important intellectual content; S.L. contributed to the conceptual design, experimental design, manuscript writing, and revisions throughout the work. All authors read and commented on the manuscript. All authors agree with the authorship change.

DECLARATION OF INTERESTS

The authors declare no conflict of interest.

STAR★METHODS

Detailed methods are provided in the online version of this paper and include the following:

- KEY RESOURCES TABLE
- EXPERIMENTAL MODEL AND STUDY PARTICIPANT DETAILS
- METHOD DETAILS
  - Preparation of graphene films
  - Preparation of the metamaterial
  - Simulation results of the metamaterials' properties
  - Mathematical modeling and numerical simulation of the actuator based on the photothermal effect
- QUANTIFICATION AND STATISTICAL ANALYSIS

SUPPLEMENTAL INFORMATION

Supplemental information can be found online at https://doi.org/10.1016/j.isci.2025.111743.

Received: July 18, 2024
Revised: September 12, 2024
Accepted: November 20, 2024
Published: January 4, 2025

REFERENCES

1. Cacucciolo, V., Shintake, J., Kuwajima, Y., Maeda, S., Floreano, D., and Shea, H. (2019). Stretchable pumps for soft machines. Nature *572*, 516–519. https://doi.org/10.1038/s41586-019-1479-6.
2. Xu, Y., Fei, Q., Page, M., Zhao, G., Ling, Y., Stoll, S.B., and Yan, Z. (2021). Paper-based wearable electronics. iScience *24*, 102736. https://doi.org/10.1016/j.isci.2021.102736.
3. Li, G., Chen, X., Zhou, F., Liang, Y., Xiao, Y., Cao, X., Zhang, Z., Zhang, M., Wu, B., Yin, S., et al. (2021). Self-powered soft robot in the Mariana Trench. Nature *591*, 66–71. https://doi.org/10.1038/s41586-020-03153-z.
4. Jiao, Z., Zhang, C., Wang, W., Pan, M., Yang, H., and Zou, J. (2019). Advanced Artificial Muscle for Flexible Material-Based Reconfigurable Soft Robots. Adv. Sci. *6*, 1901371. https://doi.org/10.1002/advs.201901371.
5. Larson, N.M., Mueller, J., Chortos, A., Davidson, Z.S., Clarke, D.R., and Lewis, J.A. (2023). Rotational multimaterial printing of filaments with sub-voxel control. Nature *613*, 682–688. https://doi.org/10.1038/s41586-022-05490-7.

6. Huang, Z., Wei, C., Dong, L., Wang, A., Yao, H., Guo, Z., and Mi, S. (2022). Fluid-driven hydrogel actuators with an origami structure. iScience *25*, 104674. https://doi.org/10.1016/j.isci.2022.104674.

7. Wehner, M., Truby, R.L., Fitzgerald, D.J., Mosadegh, B., Whitesides, G.M., Lewis, J.A., and Wood, R.J. (2016). An integrated design and fabrication strategy for entirely soft, autonomous robots. Nature *536*, 451–455. https://doi.org/10.1038/nature19100.

8. Aubin, C.A., Gorissen, B., Milana, E., Buskohl, P.R., Lazarus, N., Slipher, G.A., Keplinger, C., Bongard, J., Iida, F., Lewis, J.A., and Shepherd, R.F. (2022). Towards enduring autonomous robots via embodied energy. Nature *602*, 393–402. https://doi.org/10.1038/s41586-021-04138-2.

9. Wang, X., Jiao, N., Tung, S., and Liu, L. (2019). Photoresponsive Graphene Composite Bilayer Actuator for Soft Robots. ACS Appl. Mater. Interfaces *11*, 30290–30299. https://doi.org/10.1021/acsami.9b09491.

10. Hu, Y., Yang, L., Yan, Q., Ji, Q., Chang, L., Zhang, C., Yan, J., Wang, R., Zhang, L., Wu, G., et al. (2021). Self-Locomotive Soft Actuator Based on Asymmetric Microstructural $Ti_3C_2T_x$ MXene Film Driven by Natural Sunlight Fluctuation. ACS Nano *15*, 5294–5306. https://doi.org/10.1021/acsnano.0c10797.

11. Ni, C., Chen, D., Wen, X., Jin, B., He, Y., Xie, T., and Zhao, Q. (2023). High speed underwater hydrogel robots with programmable motions powered by light. Nat. Commun. *14*, 7672. https://doi.org/10.1038/s41467-023-43576-6.

12. Lahikainen, M., Zeng, H., and Priimagi, A. (2018). Reconfigurable photoactuator through synergistic use of photochemical and photothermal effects. Nat. Commun. *9*, 4148. https://doi.org/10.1038/s41467-018-06647-7.

13. Shi, X., Zhang, K., Chen, J., Qian, H., Huang, Y., and Jiang, B. (2024). Octopi Tentacles-Inspired Architecture Enables Self-Healing Conductive Rapid-Photo-Responsive Materials for Soft Multifunctional Actuators. Adv. Funct. Mater. *34*, 2311567. https://doi.org/10.1002/adfm.202311567.

14. Gao, Z., Zhang, X., Wu, Y., Pham, M.-S., Lu, Y., Xia, C., Wang, H., and Wang, H. (2024). Damage-programmable design of metamaterials achieving crack-resisting mechanisms seen in nature. Nat. Commun. *15*, 7373. https://doi.org/10.1038/s41467-024-51757-0.

15. Gao, Z., Wang, H., Ren, P., Zheng, G., Lu, Y., Peng, B., Tang, Z., Wu, Y., and Wang, H. (2024). Metainterfaces with mechanical, thermal, and active programming properties based on programmable orientation-distributed biometric architectonics. Mater. Horiz. *11*, 4037–4053. https://doi.org/10.1039/d4mh00570h.

16. Gemen, J., Church, J.R., Ruoko, T.P., Durandin, N., Białek, M.J., Weißenfels, M., Feller, M., Kazes, M., Odaybat, M., Borin, V.A., et al. (2023). Disequilibrating azobenzenes by visible-light sensitization under confinement. Science *381*, 1357–1363. https://doi.org/10.1126/science.adh9059.

17. Jaiswal, M., Singh, S., Sharma, B., Choudhary, S., Kumar, R., and Sharma, S.K. (2024). Sodium Niobate Nanowires Embedded PVA-Hydrogel-Based Triboelectric Nanogenerator for Versatile Energy Harvesting and Self-Powered CO Gas Sensor. Small *20*, 2403699. https://doi.org/10.1002/smll.202403699.

18. Liu, C., and Pham, M.S. (2024). Spatially Programmable Architected Materials Inspired by the Metallurgical Phase Engineering. Adv. Mater. *36*, 2305846. https://doi.org/10.1002/adma.202305846.

19. Dong, Y., Fu, Y., and Fang, D. (2024). Meso-structural optimization design of multifarious and complex fabric rubber composite structure. Int. J. Solid Struct. *290*, 112672. https://doi.org/10.1016/j.ijsolstr.2024.112672.

20. Lin, Y., Li, P., Liu, W., Chen, J., Liu, X., Jiang, P., and Huang, X. (2024). Application-Driven High-Thermal-Conductivity Polymer Nanocomposites. ACS Nano *18*, 3851–3870. https://doi.org/10.1021/acsnano.3c08467.

21. Xin, G., Yao, T., Sun, H., Scott, S.M., Shao, D., Wang, G., and Lian, J. (2015). Highly thermally conductive and mechanically strong graphene fibers. Science *349*, 1083–1087. https://doi.org/10.1126/science.aaa6502.

22. Geim, A.K. (2009). Graphene: Status and Prospects. Science *324*, 1530–1534. https://doi.org/10.1126/science.1158877.

23. Lee, G.H., Cooper, R.C., An, S.J., Lee, S., van der Zande, A., Petrone, N., Hammerberg, A.G., Lee, C., Crawford, B., Oliver, W., et al. (2013). High-Strength Chemical-Vapor Deposited Graphene and Grain Boundaries. Science *340*, 1073–1076. https://doi.org/10.1126/science.1235126.

24. Basko, D. (2011). A Photothermoelectric Effect in Graphene. Science *334*, 610–611. https://doi.org/10.1126/science.1214560.

25. Wu, S., Li, T., Tong, Z., Chao, J., Zhai, T., Xu, J., Yan, T., Wu, M., Xu, Z., Bao, H., et al. (2019). High-Performance Thermally Conductive Phase Change Composites by Large-Size Oriented Graphite Sheets for Scalable Thermal Energy Harvesting. Adv. Mater. *31*, 1905099. https://doi.org/10.1002/adma.201905099.

26. Xue, P., Valenzuela, C., Ma, S., Zhang, X., Ma, J., Chen, Y., Xu, X., and Wang, L. (2023). Highly Conductive MXene/PEDOT:PSS-Integrated Poly(N-Isopropylacrylamide) Hydrogels for Bioinspired Somatosensory Soft Actuators. Adv. Funct. Mater. *33*, 2214867. https://doi.org/10.1002/adfm.202214867.

27. Ma, S., Xue, P., Valenzuela, C., Zhang, X., Chen, Y., Liu, Y., Yang, L., Xu, X., and Wang, L. (2024). Highly Stretchable and Conductive MXene-Encapsulated Liquid Metal Hydrogels for Bioinspired Self-Sensing Soft Actuators. Adv. Funct. Mater. *34*, 2309899. https://doi.org/10.1002/adfm.202309899.

28. Leeladhar, and Singh, J.P. (2018). Photomechanical and Chemomechanical Actuation Behavior of Graphene-Poly(dimethylsiloxane)/Gold Bilayer Tube for Multimode Soft Grippers and Volatile Organic Compounds Detection Applications. ACS Appl. Mater. Interfaces *10*, 33956–33965. https://doi.org/10.1021/acsami.8b11440.

29. Xiao, J., Zhou, T., Yao, N., Ma, S., Pan, C., Wang, P., Fu, H., Liu, H., Pan, J., Yu, L., et al. (2022). Optical fibre taper-enabled waveguide photoactuators. Nat. Commun. *13*, 363. https://doi.org/10.1038/s41467-022-28021-4.

30. Chen, L., Weng, M., Zhou, P., Huang, F., Liu, C., Fan, S., and Zhang, W. (2019). Graphene-Based Actuator with Integrated-Sensing Function. Adv. Funct. Mater. *29*, 1806057. https://doi.org/10.1002/adfm.201806057.

31. Pan, X., Grossiord, N., Sol, J.A.H.P., Debije, M.G., and Schenning, A.P.H.J. (2021). 3D Anisotropic Polyethylene as Light-Responsive Grippers and Surfing Divers. Adv. Funct. Mater. *31*, 2100465. https://doi.org/10.1002/adfm.202100465.

32. Li, J., Zhang, R., Mou, L., Jung de Andrade, M., Hu, X., Yu, K., Sun, J., Jia, T., Dou, Y., Chen, H., et al. (2019). Photothermal Bimorph Actuators with In-Built Cooler for Light Mills, Frequency Switches, and Soft Robots. Adv. Funct. Mater. *29*, 1808995. https://doi.org/10.1002/adfm.201808995.

33. Seol, J.H., Jo, I., Moore, A.L., Lindsay, L., Aitken, Z.H., Pettes, M.T., Li, X., Yao, Z., Huang, R., Broido, D., et al. (2010). Two-Dimensional Phonon Transport in Supported Graphene. Science *328*, 213–216. https://doi.org/10.1126/science.1184014.

34. Heikkilä, T.T. (2022). Surprising superconductivity of graphene An ordinary graphene bilayer exhibits extraordinary superconductivity. Science *375*, 719–720. https://doi.org/10.1126/science.abn9631.

35. Song, H., Liu, J., Liu, B., Wu, J., Cheng, H.M., and Kang, F. (2018). Two-Dimensional Materials for Thermal Management Applications. Joule *2*, 442–463. https://doi.org/10.1016/j.joule.2018.01.006.

36. Ye, M., Zhang, Z., Zhao, Y., and Qu, L. (2018). Graphene Platforms for Smart Energy Generation and Storage. Joule *2*, 245–268. https://doi.org/10.1016/j.joule.2017.11.011.

37. Acome, E., Mitchell, S.K., Morrissey, T.G., Emmett, M.B., Benjamin, C., King, M., Radakovitz, M., and Keplinger, C. (2018). Hydraulically amplified self-healing electrostatic actuators with muscle-like performance. Science *359*, 61–65. https://doi.org/10.1126/science.aao6139.

38. Chen, Y., Yang, J., Zhang, X., Feng, Y., Zeng, H., Wang, L., and Feng, W. (2021). Light-driven bimorph soft actuators: design, fabrication, and properties. Mater. Horiz. *8*, 728–757. https://doi.org/10.1039/d0mh01406k.

39. Tang, R., Liu, Z., Xu, D., Liu, J., Yu, L., and Yu, H. (2015). Optical Pendulum Generator Based on Photomechanical Liquid-Crystalline Actuators. ACS Appl. Mater. Interfaces *7*, 8393–8397. https://doi.org/10.1021/acsami.5b01732.

40. Lu, X., Zhang, H., Fei, G., Yu, B., Tong, X., Xia, H., and Zhao, Y. (2018). Liquid-Crystalline Dynamic Networks Doped with Gold Nanorods Showing Enhanced Photocontrol of Actuation. Adv. Mater. *30*, 1706597. https://doi.org/10.1002/adma.201706597.

41. Zhang, X., Yu, Z., Wang, C., Zarrouk, D., Seo, J.W.T., Cheng, J.C., Buchan, A.D., Takei, K., Zhao, Y., Ager, J.W., et al. (2014). Photoactuators and motors based on carbon nanotubes with selective chirality distributions. Nat. Commun. *5*, 2983. https://doi.org/10.1038/ncomms3983.

42. Yu, Y., Peng, R., Chen, Z., Yu, L., Li, J., Wang, J., Liu, X., Wang, Q., and Wang, X. (2021). Photoresponsive Biomimetic Soft Robots Enabled by Near-Infrared-Driven and Ultrarobust Sandwich-Structured Nanocomposite Films. Adv. Intell. Syst. *3*, 2100012. https://doi.org/10.1002/aisy.202100012.

43. Chen, Z., Wang, H., Cao, Y., Chen, Y., Akkus, O., Liu, H., and Cao, C.C. (2023). Bio-inspired anisotropic hydrogels and their applications in soft actuators and robots. Matter *6*, 3803–3837. https://doi.org/10.1016/j.matt.2023.08.011.

44. Yoon, D., Son, Y.-W., and Cheong, H. (2011). Negative Thermal Expansion Coefficient of Graphene Measured by Raman Spectroscopy. Nano Lett. *11*, 3227–3231. https://doi.org/10.1021/nl201488g.

45. Awad, S.A. (2021). Mechanical and thermal characterisations of low-density polyethylene/nanoclay composites. Polym. Polym. Compos. *29*, 1325–1332. https://doi.org/10.1177/0967391120968441.

46. Lin, J., Li, Y., Yang, W., Liu, X., Huang, W., Wang, Y., and Sun, H. (2019). Molecular dynamics simulation study on the structure and properties of polyimide/silica hybrid materials. J. Appl. Polym. Sci. *136*, 47335. https://doi.org/10.1002/app.47335.

47. Zhang, Y.Y., and Gu, Y.T. (2013). Mechanical properties of graphene: Effects of layer number, temperature and isotope. Comput. Mater. Sci. *71*, 197–200. https://doi.org/10.1016/j.commatsci.2013.01.032.

48. Stefaniuk, D., and Kachanov, M. (2023). Voigt-Reuss and Hashin-Shtrikman bounds revisited. Int. J. Eng. Sci. *191*, 103903. https://doi.org/10.1016/j.ijengsci.2023.103903.

STAR★METHODS

KEY RESOURCES TABLE

REAGENT or RESOURCE	SOURCE	IDENTIFIER
Chemicals, peptides, and recombinant proteins		
graphene oxide (GO) ,50% wt.	Shanghai McLean Biochemical Technology Co. Ltd.	G10194
Low-Density Polyethylene (LDPE)	Wuhan Kaidi Co.	https://kdslzp.1688.com/
Polyimide (PI)	Xinwangyuan Co.	https://www.1688.com/factory/b2b-221090898939604ef2.html
Critical commercial assays		
scanning electron microscopy (SEM)	ZEISS	https://zeiss.com.cn
stress-strain measurements	E1000 system (EHFUV100k2-040-1A)	https://www.ssi.shimadzu.com/products/materials-testing/fatigue-testing-impact-testing/ehf-e-series/spec.html
Software and algorithms		
COMSOL Multiphysics 5.6	COMSOL Co., Ltd.	https://cn.comsol.com/
Other		
solar simulator (CEL-PE300L-3A)	Beijing Zhongjiao Jinyuan Technology Co., Ltd.	http://www.bjaulight.com/
direct electricity source SPS-3010N	JESVERTY Co.	https://www.amazon.co.uk/Jesverty-Adjustable-Switching-LED-Adjustment/dp/B0B8S6CH3H
IR camera TiS20+ MAX	FLUKE	https://www.fluke.com.cn/product/热成像相机/tis20plus

EXPERIMENTAL MODEL AND STUDY PARTICIPANT DETAILS

The model of this study is based on thermal conduction and solid mechanics models.

METHOD DETAILS

Preparation of graphene films

Fabrication of Graphene films: A commercially available 50%wt graphene oxide (GO) dispersion was diluted with ultra-pure water to a final concentration of 20 mg/mL. Subsequently, the diluted GO suspension was uniformly coated onto a poly (ethylene terephthalate) (PET) substrate, and allowed to evaporate at room temperature for 24 hours to obtain a GO assembled film. The resulting film was annealed at 1300°C for 120 minutes, followed by additional annealing at 2850°C for 60 minutes in an argon (Ar) gas environment. Finally, a flexible interlayer was achieved through a rolling process, yielding a graphene film.

Preparation of the metamaterial

The Graphene film was first thermally pasted onto LDPE film. The sandwich-structured PI/Graphene/LDPE film was obtained by pasting the PI adhesive on the Graphene-plated LDPE film. As a reference, PI/LDPE composite film with Graphene layer coating was also prepared by directly pasting a PI adhesive on the surface of a LDPE film. Fabrication of the film was done at room temperature (25 $^{\circ}C$) and the original sandwich structured PI/Graphene/LDPE film was flat. Fabrication of Photo responsive PI/Graphene/LDPE Actuators: Evaluation of the photo responsive actuation behavior of the sandwich-structured PI/Graphene/LDPE film was conducted on tailored films, in which large-sized sandwich-structured PI/Au/LDPE films were cut into rectangle pieces with 10 *mm* in width and 50 *mm* in length.

Simulation results of the metamaterials' properties

The influence of different temperatures and thicknesses of each layer on the curvature of the sandwich-structured actuators can be calculated by the classical bimorph theory model. The formula is expressed as follow:

$$\kappa = \frac{6W_1W_2E_1E_2t_1t_2(t_1+t_2)(\alpha_1-\alpha_2)}{\left(W_1E_1t_1^2\right)^2+\left(W_2E_2t_2^2\right)^2+2W_1W_2E_1E_2t_1t_2\left(2t_1^2+3t_1t_2+2t_2^2\right)}(T-T_{ref}) \quad \text{(Equation 1)}$$

In this formula, κ is the actuator's curvature, W_1, W_2 are its widths, E_1, E_2 are the young's modulus of LDPE and PI, t_1, t_2 are the thickness of these two materials, α_1, α_2 are the CTEs, T is the actuator's temperature, T_{ref} is the reference temperature. Besides, considering that young's modulus and CTE will change with temperature, these two effects can't be ignored when calculating curvature.[42,44–48] The stiffness (Young's Modulus) of the whole system is affected by two factors: temperatures and the thicknesses of layers. With regard to the influence of thickness, the Voigt-Reuss-Hill (VRH)[48] mixed rule is used to estimate the overall young's modulus.

$$\begin{cases} E_V = \sum_{i=1}^{n} f_i \cdot E_i \\ \frac{1}{E_R} = \sum_{i=1}^{n} \frac{f_i}{E_i} \\ E = (E_V + E_R)/2 \end{cases} \quad \text{(Equation 2)}$$

Where E_V is the Voigt limit, E_R is the Reuss limit, f is the volume fraction, E is the Young's Modulus, this method which takes into account two extreme cases provides a more accurate result. Based on the summarized patterns identified in the preceding text, 20μm of LDPE layer, 30μm of PI layer and 6μm of Graphene's have been chose. Subsequently, an in-depth investigation into the actuator produced based on this dimension will be conducted. This involves meticulous supplementation of simulated numerical values for the stiffness and curvature of the modified actuator.

Mathematical modeling and numerical simulation of the actuator based on the photothermal effect

The establishment of the geometric model and the setting of parameters will not be elaborated upon, as everyone has their own methods for these. This section mainly introduces the constraints and boundary conditions during the computation process.

After setting the material properties, it is necessary to set the initial conditions and boundary conditions of the model.

(1) In the model builder, select "Solid Mechanics" under "Linear Elastic Material", right-click to add the thermal expansion interface, and select all domains for the region. Set the volumetric reference temperature to 293.15 K, set the temperature to T+273.15 K, and keep other settings as default
(2) Add a fixed-point constraint to fix the line segment as shown in Figure S5A, and keep other settings as default
(3) Add gravity as shown in Figure S5B, and keep other settings as default

In COMSOL Multiphysics, the motion of the actuator is simulated using the Solid Mechanics module with the thermal expansion interface. It is necessary to add the thermal expansion interface and set the initial conditions and boundary conditions before simulating the actuator's behavior at different temperatures. The governing equation for the linear elastic material model is:

$$-\nabla\sigma = F_V \quad \text{(Equation 3)}$$

Where, $\sigma = s$ represents the stress, F_V is the body force, and the stress-strain relationship at this time is:

$$s = s^0 + C(\varepsilon - \varepsilon_{th} - \varepsilon_0) \quad \text{(Equation 4)}$$

In the equation, s^0 is the initial stress, in Pa (Pascals),
ε_0 is the initial strain variable, in meters,
C is the elasticity matrix,
ε is the total strain variable, in meters,
ε_{th} is the thermal strain variable, in meters.
The total strain variable ε is a function of the volumetric displacement of the actuator's motion and can be expressed as:

$$\varepsilon = \frac{1}{2}\left(\nabla \boldsymbol{u} + \nabla \boldsymbol{u}^T\right) \quad \text{(Equation 5)}$$

In the equation, $\boldsymbol{u}$ represents the volumetric displacement of the actuator, and the thermal strain can be determined by the following formula:

$$\varepsilon_{th} = \alpha(T)(T - T_{ref}) \quad \text{(Equation 6)}$$

where, $\alpha(T)$ is the coefficient of thermal expansion of the material, which is a function of the operating temperature, T is the temperature acting on the actuator, T_{ref} is the reference temperature (in this work, it is 20°C).

QUANTIFICATION AND STATISTICAL ANALYSIS

Statistical analysis of data was performed using Excel (Microsoft) and Origin (Origin Lab).